Variational Bayesian Blind Color Deconvolution of Histopathological Images

Natalia Hidalgo-Gavira, Javier Mateos, *Senior Member, IEEE*, Miguel Vega, Rafael Molina, *Senior Member, IEEE*, Aggelos K. Katsaggelos, *Fellow, IEEE*

Abstract—Most whole-slide histological images are stained with two or more chemical dyes. Slide stain separation or color deconvolution is a crucial step within the digital pathology workflow. In this paper, the blind color deconvolution problem is formulated within the Bayesian framework. Starting from a multi-stained histological image, our model takes into account both spatial relations among the concentration image pixels and similarity between a given reference color-vector matrix and the estimated one. Using Variational Bayes inference, three efficient new blind color deconvolution methods are proposed which provide automated procedures to estimate all the model parameters in the problem. A comparison with classical and current state-of-the-art color deconvolution algorithms using real images has been carried out demonstrating the superiority of the proposed approach.

Index Terms—Blind color deconvolution, histopathological images, Bayesian modelling and inference, variational Bayes

I. INTRODUCTION

In digital brightfield microscopy, tissues are usually stained to enhance particular components of cellular structures before digitization and evaluation by pathologists. Hematoxylin and Eosin (H&E) probably form the most widely used combination of stains. Hematoxylin stains cell nuclei blue while its counterstain eosin makes the cytoplasm and stromal components look in various shades of red/pink.

Even when using the same combination of stains, color variations, which are not due to the different content of the acquired tissue samples, occur. They are due to the use of different scanners, stain manufacturers, or staining procedures, among other factors. In spite of these color variations, pathologists are able to visually analyze the stained images. Unfortunately, such variations can hamper the performance of Computer-Aided Diagnosis (CAD) systems. While pathologists are able to visually analyze multi-color stained images, CAD systems usually make use of the information provided by the different stains separately. This information is specially important as the amount of stain absorbed by a sample is used to quantitatively determine the presence of cancerous cells in the tissue [1].

Natalia Hidalgo-Gavira, Javier Mateos and Rafael Molina are with Dpto. de Ciencias de la Computación e I. A., Universidad de Granada, Spain
Miguel Vega is with Dpto. de Lenguajes y Sistemas Informáticos, Universidad de Granada, Spain
Aggelos Katsaggelos is with Dept. of Electrical Engineering and Computer Science, Northwestern University, Evanston, IL, USA

Color deconvolution (CD) aims at separating a color image into the concentration of each stain present in it, as well as at estimating the spectral properties for each stain. This is not an easy task since the exact spectral profile of the stains varies from one image to another [2]. Hence, a process of color normalization is usually used to reduce the color variation effects by transforming the color of all input images to a single target image colors. This is usually done by color deconvolving each source image, replacing the source stain color-vectors with the target stain vectors obtained from the reference slide, and converting the calculated concentrations back to an RGB image.

Over the years, several CD methods have been proposed (see [3] for a recent review of classical and state-of-the-art CD methods). One of the first CD methods was proposed by Ruifrok *et al.* [4]. This supervised method maps the RGB image into the optical density (OD) space, where the values are linear with the concentration of absorbing material. Then, using slides stained with a single dye, the relative absorption of each color is measured and used as the color-vector for the dye. This is a supervised manual process, tedious and prone to errors. Ideally, this process has to be performed on each image. However, Ruifrok *et al.* [4] propose the use of a set of stain color-vectors for hematoxylin, eosin, and 3,3'-Diaminobenzidine (DAB) stains, calibrated for processing and digitization in their laboratory. Note that this model does not take into account inter-slide variability, which may result in a poor separation. Several unsupervised methods have been proposed to tackle inter-slide variability. In [1] the problem is formulated as a blind source separation one which is solved by Non-negative Matrix Factorization (NMF) and Independent Component Analysis (ICA). In [5] SVD corrected for robustness was proposed to separate H&E stained images.

More recently, in [6] the stain color vectors are estimated by projecting the input color image onto the Maxwellian chromaticity plane to form clusters, each one corresponding to one stained tissue type. In [7] color normalization is performed by first deconvolving both source and target images, applying a non-linear mapping of the source to the target image channels and recombining the mapped channels into the normalized source image. In order to build the stain color-vector matrix, the image is segmented into background and pixels belonging to each stain using supervised relevant vector machines. The mean color of the pixels in each class is utilized as the stain color-vector. A segmentation based approach is also used in [8]. The input image is segmented by first detecting nuclei using the Hough transform and then thresholding the

image to separate eosin and background. After removing the background, the image is segmented by using a k-NN classifier trained using random samples from hematoxylin and eosin classes. McCann *et al.* [9] extend the method in [5] by adjusting the contrast of the eosin channel and including interaction between eosin and hematoxylin in the pixels of the hematoxylin channel where the eosin value had been changed. The algorithm is tested on a set of three H&E images stained and destained to create H-only and E-only images which can be used as ground-truth separated images for the H&E image. The NMF method in [1] is extended in [10] with regularization and sparsity terms which aim to represent the image using fewer "active" components for better interpreting the staining of different components. A similar sparse NMF method is proposed by Vahadane *et al.* [11] for color normalization. The use of Non-Negative Least Squares (NNLS) instead of NMF is proposed in [12] resulting in a faster and less memory demanding method. Alsubaie *et al.* [13], [14], following [15], propose the use of ICA in the wavelet domain where the independence condition among sources is relaxed. Astola [16] states that the method in [5] obtains better results applied in the linearly inverted RGB-space and not in the (logarithmically inverted) absorbency space. In [17] the authors introduce a loss function based on their experience which is optimized to obtain the image stain color-vectors. These vectors are later used to normalize the input image as if it had been obtained using a target color-vector matrix.

Most of the previously described methods use CD prior to color normalization. Some deep learning methods introduce deconvolution or normalization layers that are applied before a classification network [18], [19]. Deep learning methods which use sparse autoencoders [20] or generative adversarial networks [21], [22] have been recently proposed. They normalize the input image to a target image in a fully unsupervised manner. These deep learning methods, however, do not output the separated stains.

In this paper we advance on the works already presented in [23], [24] and propose, depending on the information available, three CD methods that simultaneously estimate the color-vector matrix, the concentration of the stains, and all required model parameters. A full probabilistic modelling of all the involved latent variables (including model parameters) is provided together with detailed derivations of all the needed quantities and posterior distributions. In our blind CD problem formulation we introduce prior knowledge in three different ways. Firstly, a smoothness prior model on each one of the stain concentrations which helps reduce the acquisition noise and takes into account the spatial correlation between adjacent pixels. Secondly, we take into account that the color-vector matrices are often assumed to be close to a commonly accepted standard matrix or to a laboratory dependant matrix and introduce this information in the model. Finally, since the observation and prior models depend on parameters (which are frequently termed hyper-parameters) we describe how information on them can be introduced. Variational Bayes inference [25], [26], [27], [28] is used to provide our solutions to the CD problem. The performance of the proposed algorithms is evaluated both visually and numerically on different image datasets, from different tissues and laboratories. This evaluation extends the results already presented in [23], [24] and provide evidence of the quality of the proposed algorithms.

The rest of the paper is organized as follows: in section II we mathematically formulate the blind CD of histopathological images problem. This problem is approached using the Bayesian framework in III. In this section we also carry out Bayesian inference to estimate the color-vector matrix, concentrations, and model parameters in a fully automated manner. In Sect. IV, two sets of H&E stained images used for evaluation as well as the evaluation procedure are described. The proposed methods performance is compared with other classical and state-of-the-art CD methods in Sect. V. Finally, Sect. VI concludes the paper.

II. PROBLEM FORMULATION

A stained histological specimen's slide digitized by a bright-field microscope is stored as a RGB intensity image with M rows and N columns, that is, with MN pixels, represented by the $MN \times 3$ matrix,

$$\mathbf{I} = \begin{bmatrix} i_{1R} & i_{1G} & i_{1B} \\ \vdots & \vdots & \vdots \\ i_{MNR} & i_{MNG} & i_{MNB} \end{bmatrix} = \begin{bmatrix} \mathbf{i}_{1,:}^{\mathrm{T}} \\ \vdots \\ \mathbf{i}_{MN,:}^{\mathrm{T}} \end{bmatrix} = \begin{bmatrix} \mathbf{i}_R & \mathbf{i}_G & \mathbf{i}_B \end{bmatrix} . \tag{1}$$

Each value i_{ic} of the image is the transmitted light across the slide. For diagnostic purposes, however, the interest is centered on the contribution of each stain to this value, that is, its absorbency or *optical density* (OD). The OD for channel c of the slide, $\mathbf{y}_c \in \mathbb{R}^{MN \times 1}$, is

$$\mathbf{y}_c = -\log_{10}\left(\frac{\mathbf{i}_c}{\mathbf{i}_c^0}\right), \tag{2}$$

where $\mathbf{i}_c^0$ denotes the incident light, and the division operation and $\log_{10}(\cdot)$ function are computed element-wise. The observed OD image $\mathbf{Y} \in \mathbb{R}^{MN \times 3}$ is composed by the RGB OD channels, i.e., $\mathbf{Y} = [\mathbf{y}_R, \mathbf{y}_G, \mathbf{y}_B]$.

According to the monochromatic Beer-Lambert law [4], the OD of a slide stained with n_s stains $\mathbf{Y}$ can be obtained from

$$\mathbf{Y}^{\mathrm{T}} = \mathbf{M}\mathbf{C}^{\mathrm{T}} + \mathbf{N}^{\mathrm{T}}, \tag{3}$$

where $\mathbf{N}$ is a random matrix of size $MN \times 3$ with i.i.d. zero mean Gaussian components with variance β^{-1}, $\mathbf{C} \in \mathbb{R}^{MN \times n_s}$ is the stain concentration matrix

$$\mathbf{C} = \begin{bmatrix} c_{11} & \cdots & c_{1n_s} \\ \vdots & \ddots & \vdots \\ c_{MN1} & \cdots & c_{MNn_s} \end{bmatrix} = \begin{bmatrix} \mathbf{c}_{1,:}^{\mathrm{T}} \\ \vdots \\ \mathbf{c}_{MN,:}^{\mathrm{T}} \end{bmatrix} = \begin{bmatrix} \mathbf{c}_1 & \cdots & \mathbf{c}_{n_s} \end{bmatrix}, \tag{4}$$

with the i-th row $\mathbf{c}_{i,:}^{\mathrm{T}} = (c_{i1}, \ldots, c_{in_s})$. $i = 1, \ldots, MN$ representing the contribution of the stains to the i-th pixel value and the s-th column $\mathbf{c}_s = (c_{1s}, \ldots, c_{MNs})^{\mathrm{T}}$, $s \in \{1, \ldots, n_s\}$ representing the s-th stain concentrations, and $\mathbf{M} \in \mathbb{R}^{3 \times n_s}$ is the normalized stains' specific color-vector matrix

$$\mathbf{M} = \begin{bmatrix} m_{R1} & \cdots & m_{Rn_s} \\ m_{G1} & \cdots & m_{Gn_s} \\ m_{B1} & \cdots & m_{Bn_s} \end{bmatrix} = \begin{bmatrix} \mathbf{m}_{R,:}^{\mathrm{T}} \\ \mathbf{m}_{G,:}^{\mathrm{T}} \\ \mathbf{m}_{B,:}^{\mathrm{T}} \end{bmatrix} = \begin{bmatrix} \mathbf{m}_1 & \cdots & \mathbf{m}_{n_s} \end{bmatrix}. \tag{5}$$

Each column, $\mathbf{m}_s$, in matrix $\mathbf{M}$ is a unit $\ell2$ norm stain color-vector containing the relative RGB color composition of the corresponding stain in the OD space.

Color Deconvolution (CD) is a technique that allows to obtain the stain concentration matrix, $\mathbf{C}$, and the color-vector matrix, $\mathbf{M}$, from the observed optical densities, $\mathbf{Y}$. In the following section we will use Bayesian modeling and inference to estimate $\mathbf{M}$ and $\mathbf{C}$ as well as the model parameters.

III. BAYESIAN MODELLING AND INFERENCE

Following the degradation model in (3), we have

$$
\begin{aligned}
\mathrm{p}(\mathbf{Y}|\mathbf{C}, \mathbf{M}, \beta) &= \prod_{i=1}^{MN} \mathrm{p}(\mathbf{y}_{i,:}|\mathbf{M}, \mathbf{c}_{i,:}, \beta) \\
&= \prod_{i=1}^{MN} \mathcal{N}(\mathbf{y}_{i,:}|\mathbf{M}\mathbf{c}_{i,:}, \beta^{-1}\mathbf{I}_{3\times 3}) \\
&\propto \prod_{i=1}^{MN} \beta^{\frac{3}{2}} \exp\left(-\frac{1}{2}\beta\|\mathbf{y}_{i,:} - \mathbf{M}\mathbf{c}_{i,:}\|^2\right). \quad (6)
\end{aligned}
$$

The stain concentrations at each pixel on the image are expected to have values similar to the ones of the surrounding pixels. This prior information is commonly used in image processing by the introduction of a Simultaneous Autorregresive (SAR) prior model. This model has been successfully used in other inverse problems such as image restoration [29] or super-resolution [30]. Hence, we impose smoothing prior models on the concentrations $\mathbf{c}_s$, $s = 1, \ldots, n_s$, that is, on the columns of $\mathbf{C}$, as

$$
\mathrm{p}(\mathbf{C}|\boldsymbol{\alpha}) = \prod_{s=1}^{n_s} \mathrm{p}(\mathbf{c}_s|\alpha_s) \propto \prod_{s=1}^{n_s} \alpha_s^{\frac{MN}{2}} \exp\left(-\frac{1}{2}\alpha_s \mathbf{c}_s^{\mathrm{T}}\mathbf{F}^{\mathrm{T}}\mathbf{F}\mathbf{c}_s\right),
$$
$$(7)$$

where $\mathbf{F} \in \mathbb{R}^{MN \times MN}$ is a high pass filter, usually a 2D Laplacian filter, and α_s, $s = 1, \ldots, n_s$, controls the amount of smoothness. Note that smoothness is imposed in each one of the concentration channels independently since each dye stains different structures of the histological image.

The color-vector matrix $\mathbf{M} = [\mathbf{m}_1, \ldots, \mathbf{m}_{n_s}]$ is also unknown because it depends on many factors that include the staining procedures and microscopes. In [4], standard color-vectors for hematoxylin, eosin, and DAB stains were proposed. Laboratory dependant color-vectors could be obtained following a similar procedure. Although those laboratory or standard color-vectors are not usually exact for each single image, they are very representative and have been frequently used. In this paper we incorporate the similarity to a reference color-vector matrix $\underline{\mathbf{M}} = [\underline{\mathbf{m}}_1, \ldots, \underline{\mathbf{m}}_{n_s}]$ into the prior model on $\mathbf{M}$, as

$$
\mathrm{p}(\mathbf{M}|\boldsymbol{\gamma}) = \prod_{s=1}^{n_s} \mathrm{p}(\mathbf{m}_s|\gamma_s) \propto \prod_{s=1}^{n_s} \gamma_s^{\frac{3}{2}} \exp\left(-\frac{1}{2}\gamma_s\|\mathbf{m}_s - \underline{\mathbf{m}}_s\|^2\right)
$$
$$(8)$$

where γ_s, $s = 1, \ldots, n_s$, controls our confidence on the accuracy of $\underline{\mathbf{m}}_s$.

With all these ingredients, the joint probability distribution for our problem is

$$
\begin{aligned}
&\mathrm{p}(\mathbf{Y}, \mathbf{C}, \mathbf{M}, \beta, \boldsymbol{\alpha}, \boldsymbol{\gamma}) \\
&= \mathrm{p}(\mathbf{Y}|\mathbf{C}, \mathbf{M}, \beta)\,\mathrm{p}(\mathbf{C}|\boldsymbol{\alpha})\,\mathrm{p}(\mathbf{M}|\boldsymbol{\gamma})\,\mathrm{p}(\beta)\,\mathrm{p}(\boldsymbol{\alpha})\,\mathrm{p}(\boldsymbol{\gamma}), \quad (9)
\end{aligned}
$$

where $\mathrm{p}(\boldsymbol{\gamma})$, $\mathrm{p}(\boldsymbol{\alpha})$ and $\mathrm{p}(\beta)$ are improper distributions of the form $\mathrm{p}(w) \propto \mathrm{const}$. Note that we can introduce additional information on these parameters by using gamma instead of improper priors on them. However, this has not been needed in our experiments since enough data is available as to guide the estimation procedure.

Following the Bayesian paradigm, inference will be based on the posterior distribution

$$
\mathrm{p}(\mathbf{C}, \mathbf{M}, \beta, \boldsymbol{\alpha}, \boldsymbol{\gamma}|\mathbf{Y}) = \frac{\mathrm{p}(\mathbf{Y}, \mathbf{C}, \mathbf{M}, \beta, \boldsymbol{\alpha}, \boldsymbol{\gamma})}{\mathrm{p}(\mathbf{Y})}. \quad (10)
$$

Since the above posterior cannot be obtained in closed form, several approaches have been proposed to approximate it (see, for instance, [31] for a review in the similar problem of blind image deconvolution).

Let

$$
\begin{aligned}
\boldsymbol{\Theta} &= \{\mathbf{C}, \mathbf{M}, \beta, \boldsymbol{\alpha}, \boldsymbol{\gamma}\} \quad (11) \\
&= \{\mathbf{c}_1, \ldots, \mathbf{c}_{n_s}, \mathbf{m}_1, \ldots, \mathbf{m}_{n_s}, \beta, \alpha_1, \ldots, \alpha_{n_s}, \gamma_1, \ldots, \gamma_{n_s}\}.
\end{aligned}
$$

In this paper we use the mean-field variational Bayesian model [32] to approximate $\mathrm{p}(\mathbf{C}, \mathbf{M}, \beta, \boldsymbol{\alpha}, \boldsymbol{\gamma}|\mathbf{Y})$ by the distribution $\mathrm{q}(\mathbf{C}, \mathbf{M}, \beta, \boldsymbol{\alpha}, \boldsymbol{\gamma})$ of the form

$$
\mathrm{q}(\boldsymbol{\Theta}) = \prod_{s=1}^{n_s} \mathrm{q}(\mathbf{m}_s) \prod_{s=1}^{n_s} \mathrm{q}(\mathbf{c}_s)\mathrm{q}(\beta) \prod_{s=1}^{n_s} \mathrm{q}(\alpha_s) \prod_{s=1}^{n_s} \mathrm{q}(\gamma_s), \quad (12)
$$

where $\mathrm{q}(\beta), \mathrm{q}(\alpha_s), \mathrm{q}(\gamma_s)$ $s = 1, \ldots, n_s$ are assumed to be degenerate distributions, that minimizes the Kullback-Leibler divergence defined as

$$
\begin{aligned}
\mathbf{KL}\left(\mathrm{q}(\boldsymbol{\Theta})\,\|\,\mathrm{p}(\boldsymbol{\Theta}|\mathbf{Y})\right) &= \int \mathrm{q}(\boldsymbol{\Theta}) \log \frac{\mathrm{q}(\boldsymbol{\Theta})}{\mathrm{p}(\boldsymbol{\Theta}|\mathbf{Y})}\,\mathrm{d}\boldsymbol{\Theta} \\
&= \int \mathrm{q}(\boldsymbol{\Theta}) \log \frac{\mathrm{q}(\boldsymbol{\Theta})}{\mathrm{p}(\boldsymbol{\Theta}, \mathbf{Y})}\,\mathrm{d}\boldsymbol{\Theta} + \mathrm{const},
\end{aligned}
$$
$$(13)$$

The Kullback-Leibler divergence is always non negative and equal to zero if and only if $\mathrm{q}(\boldsymbol{\Theta}) = \mathrm{p}(\boldsymbol{\Theta}|\mathbf{Y})$.

It can then be shown [32] that for each unknown $\theta \in \boldsymbol{\Theta}$, $\mathrm{q}(\theta)$ will have the form

$$
\mathrm{q}(\theta) \propto \exp \langle \log \mathrm{p}(\mathbf{Y}, \mathbf{C}, \mathbf{M}, \beta, \boldsymbol{\alpha}, \boldsymbol{\gamma}) \rangle_{\mathrm{q}(\boldsymbol{\Theta}\backslash\theta)}, \quad (14)
$$

where $\boldsymbol{\Theta}\backslash\theta$ represents all the variables in $\boldsymbol{\Theta}$ except θ and $\langle\cdot\rangle_{\mathrm{q}(\boldsymbol{\Theta}\backslash\theta)}$ denotes the expected value calculated using the distribution $\mathrm{q}(\boldsymbol{\Theta}\backslash\theta)$. For variables with a degenerate posterior approximation, that is, for $\theta \in \{\beta, \alpha_1, \ldots, \alpha_{n_s}, \gamma_1, \ldots, \gamma_{n_s}\}$, the value where the posterior degenerates is

$$
\hat{\theta} = \arg\max_{\theta} \langle \log \mathrm{p}(\mathbf{Y}, \mathbf{C}, \mathbf{M}, \beta, \boldsymbol{\alpha}, \boldsymbol{\gamma}) \rangle_{\mathrm{q}(\boldsymbol{\Theta}\backslash\theta)}. \quad (15)
$$

We would like to mention here that instead of using independent degenerate posterior distributions for these parameters we could have assigned a free form to each of them obtaining, in this case, gamma posterior approximations. We have not found it necessary in the carried out experiments.

For the rest of the variables, that is, for $\theta \in \{\mathbf{m}_1, \ldots, \mathbf{m}_{n_s}, \mathbf{c}_1, \ldots, \mathbf{c}_{n_s}\}$, when point estimates are required

$$\hat{\theta} = \langle \theta \rangle_{q(\theta)} \qquad (16)$$

is used.

Let us now obtain the analytic expressions for each unknown posterior approximation.

A. Concentration Update

To estimate the s-th stain concentration, we need to calculate, according to (14), the distribution for $\mathbf{c}_s$

$$q(\mathbf{c}_s) \propto \exp \langle \log p(\mathbf{Y}, \mathbf{C}, \mathbf{M}, \beta, \boldsymbol{\alpha}, \boldsymbol{\gamma}) \rangle_{q(\boldsymbol{\Theta} \backslash \mathbf{c}_s)}$$
$$= \exp \langle \log p(\mathbf{Y}|\mathbf{C}, \mathbf{M}, \beta) + \log p(\mathbf{C}|\boldsymbol{\alpha}) \rangle_{q(\boldsymbol{\Theta} \backslash \mathbf{c}_s)}, \qquad (17)$$

where

$$\log p(\mathbf{Y}|\mathbf{C}, \mathbf{M}, \beta) = \sum_{i=1}^{MN} \left(-\frac{1}{2}\beta \|\mathbf{y}_{i,:} - \mathbf{M}\mathbf{c}_{i,:}\|^2 \right) + \text{const}$$

$$= -\frac{\beta}{2} \sum_{i=1}^{MN} \sum_{s=1}^{n_s} \left[-2c_{is}\mathbf{m}_s^{\mathrm{T}} \left(\mathbf{y}_{i,:} - \sum_{k \neq s} c_{ik}\mathbf{m}_k \right) \right.$$
$$\left. + c_{is}^2 \|\mathbf{m}_s\|^2 \right] + \text{const}, \qquad (18)$$

$$\log p(\mathbf{C}|\boldsymbol{\alpha}) = -\frac{1}{2}\alpha_s \mathbf{c}_s^{\mathrm{T}} \mathbf{F}^{\mathrm{T}} \mathbf{F} \mathbf{c}_s + \text{const}. \qquad (19)$$

where const in the above two equations indicates terms which do not depend on $\mathbf{c}_s$. Note that in (18) we just rewrote the norm term as the sum of the terms that do not depend on c_{is} plus the term that depends on c_{is}.

We then calculate the contribution of the s-th stain to the observation, that is, we remove from the observation the contribution provided by the other stains, as

$$\mathbf{e}_{i,:}^{-s} = \mathbf{y}_{i,:} - \sum_{k \neq s} \langle c_{ik} \rangle \langle \mathbf{m}_k \rangle, \quad i = 1, \ldots, MN. \qquad (20)$$

Finally, we define

$$z_i^{-s} = \langle \mathbf{m}_s \rangle^{\mathrm{T}} \mathbf{e}_{i,:}^{-s}, \quad i = 1, \ldots, MN, \qquad (21)$$

and from (14) and (17) we have

$$\langle \log p(\mathbf{Y}, \mathbf{C}, \mathbf{M}|\beta, \boldsymbol{\alpha}, \boldsymbol{\gamma}) \rangle_{q(\boldsymbol{\Theta} \backslash \mathbf{c}_s)} = -\frac{1}{2}\alpha_s \mathbf{c}_s^{\mathrm{T}} \mathbf{F}^{\mathrm{T}} \mathbf{F} \mathbf{c}_s$$
$$- \frac{\beta}{2} \left(\|\mathbf{c}_s\|^2 \langle \|\mathbf{m}_s\|^2 \rangle - 2\mathbf{c}_s^{\mathrm{T}}\mathbf{z}^{-s} \right) + \text{const}, \qquad (22)$$

which is a quadratic form that is the exponent of a normal distribution. Therefore, from (17), it produces $q(\mathbf{c}_s) = \mathcal{N}(\mathbf{c}_s | \langle \mathbf{c}_s \rangle, \boldsymbol{\Sigma}_{\mathbf{c}_s})$, where the mean and inverse of the covariance matrix are obtained by differentiating (22), producing

$$\boldsymbol{\Sigma}_{\mathbf{c}_s}^{-1} = \beta \langle \|\mathbf{m}_s\|^2 \rangle \mathbf{I}_{MN \times MN} + \alpha_s \mathbf{F}^{\mathrm{T}} \mathbf{F}$$
$$\langle \mathbf{c}_s \rangle = \beta \boldsymbol{\Sigma}_{\mathbf{c}_s} \mathbf{z}^{-s}. \qquad (23)$$

B. Color-Vector Update

In a similar way, we calculate the distribution of $\mathbf{m}_s$,

$$q(\mathbf{m}_s) \propto \exp \langle \log p(\mathbf{Y}, \mathbf{C}, \mathbf{M}, \beta, \boldsymbol{\alpha}, \boldsymbol{\gamma}) \rangle_{q(\boldsymbol{\Theta} \backslash \mathbf{m}_s)}$$
$$= \exp \langle \log p(\mathbf{Y}|\mathbf{C}, \mathbf{M}, \beta) + \log p(\mathbf{M}|\boldsymbol{\gamma}) \rangle_{q(\boldsymbol{\Theta} \backslash \mathbf{m}_s)}, \qquad (24)$$

where $\log p(\mathbf{Y}|\mathbf{C}, \mathbf{M}, \beta)$ is defined in (18) and

$$\log p(\mathbf{M}|\boldsymbol{\gamma}) = -\frac{1}{2}\gamma_s \|\mathbf{m}_s - \underline{\mathbf{m}}_s\|^2 + \text{const}, \qquad (25)$$

where const in the above indicates terms which do not depend on $\mathbf{m}_s$. Using (20), from (14) and (24) we now have

$$\langle \log p(\mathbf{Y}, \mathbf{C}, \mathbf{M}|\beta, \boldsymbol{\alpha}, \boldsymbol{\gamma}) \rangle_{q(\boldsymbol{\Theta} \backslash \mathbf{m}_s)} = -\frac{1}{2}\gamma_s \|\mathbf{m}_s - \underline{\mathbf{m}}_s\|^2$$
$$- \frac{\beta}{2} \left(\|\mathbf{m}_s\|^2 \sum_{i=1}^{MN} \langle c_{is}^2 \rangle - 2\mathbf{m}_s^{\mathrm{T}} \sum_{i=1}^{MN} \langle c_{is} \rangle \mathbf{e}_{i,:}^{-s} \right) + \text{const}, \qquad (26)$$

which, from (24), is the exponent of the normal distribution

$$q(\mathbf{m}_s) = \mathcal{N}(\mathbf{m}_s | \langle \mathbf{m}_s \rangle, \boldsymbol{\Sigma}_{\mathbf{m}_s}), \qquad (27)$$

where its mean and inverse of covariance matrix are obtained by differentiating (26), producing

$$\boldsymbol{\Sigma}_{\mathbf{m}_s}^{-1} = \left(\beta \sum_{i=1}^{MN} \langle c_{is}^2 \rangle + \gamma_s \right) \mathbf{I}_{3 \times 3}, \qquad (28)$$

$$\langle \mathbf{m}_s \rangle = \boldsymbol{\Sigma}_{\mathbf{m}_s} \left(\beta \sum_{i=1}^{MN} \langle c_{is} \rangle \mathbf{e}_{i,:}^{-s} + \gamma_s \underline{\mathbf{m}}_s \right). \qquad (29)$$

Notice that $\langle \mathbf{m}_s \rangle$ may not be an unitary vector even if $\underline{\mathbf{m}}_s$ is. We can always replace $\langle \mathbf{m}_s \rangle$ by $\langle \mathbf{m}_s \rangle / \|\langle \mathbf{m}_s \rangle\|$ and $\boldsymbol{\Sigma}_{\mathbf{m}_s}$ by $\boldsymbol{\Sigma}_{\mathbf{m}_s} / \|\langle \mathbf{m}_s \rangle\|^2$. Notice also that $\langle c_{is}^2 \rangle$ can be calculated using (23) and $\langle \|\mathbf{m}_s\|^2 \rangle$ can be easily calculated from (29) resulting in

$$\sum_{i=1}^{MN} \langle c_{is}^2 \rangle = \sum_{i=1}^{MN} \langle c_{is} \rangle^2 + \text{tr}(\boldsymbol{\Sigma}_{\mathbf{c}_s}), \qquad (30)$$

$$\langle \|\mathbf{m}_s\|^2 \rangle = \|\langle \mathbf{m}_s \rangle\|^2 + \text{tr}(\boldsymbol{\Sigma}_{\mathbf{m}_s}). \qquad (31)$$

C. Parameter Update

Finally, noise, concentration, and color-vectors parameters, $\theta \in \{\beta, \alpha_1, \ldots, \alpha_{n_s}, \gamma_1, \ldots, \gamma_{n_s}\}$, are estimated using Eq. (15) obtaining

$$\hat{\beta} = \frac{3MN}{\text{tr}(\langle (\mathbf{Y}^{\mathrm{T}} - \mathbf{M}\mathbf{C}^{\mathrm{T}})(\mathbf{Y}^{\mathrm{T}} - \mathbf{M}\mathbf{C}^{\mathrm{T}})^{\mathrm{T}} \rangle_{q(\boldsymbol{\Theta})})}, \qquad (32)$$

$$\hat{\alpha}_s = \frac{MN}{\text{tr}(\mathbf{F}^{\mathrm{T}}\mathbf{F} \langle \mathbf{c}_s \mathbf{c}_s^{\mathrm{T}} \rangle)}, \qquad (33)$$

$$\hat{\gamma}_s = \frac{3}{\text{tr}(\langle (\mathbf{m}_s - \underline{\mathbf{m}}_s)(\mathbf{m}_s - \underline{\mathbf{m}}_s)^{\mathrm{T}} \rangle)}. \qquad (34)$$

Notice that the traces involved in the above equations can be easily calculated as

$$
\begin{aligned}
\operatorname{tr} & \left\langle (\mathbf{Y}^{\mathrm{T}} - \mathbf{M}\mathbf{C}^{\mathrm{T}})(\mathbf{Y}^{\mathrm{T}} - \mathbf{M}\mathbf{C}^{\mathrm{T}})^{\mathrm{T}} \right\rangle_{q(\Theta)} = \\
& = \operatorname{tr}((\mathbf{Y}^{\mathrm{T}} - \langle\mathbf{M}\rangle\langle\mathbf{C}\rangle^{\mathrm{T}})(\mathbf{Y}^{\mathrm{T}} - \langle\mathbf{M}\rangle\langle\mathbf{C}\rangle^{\mathrm{T}})^{\mathrm{T}}) \\
& + \sum_{s=1}^{n_s} \langle\mathbf{m}_s\rangle^{\mathrm{T}}\langle\mathbf{m}_s\rangle \operatorname{tr}(\boldsymbol{\Sigma}_{\mathbf{c}_s}) + \sum_{s=1}^{n_s} \langle\mathbf{c}_s\rangle^{\mathrm{T}}\langle\mathbf{c}_s\rangle \operatorname{tr}(\boldsymbol{\Sigma}_{\mathbf{m}_s}) \\
& + \sum_{s=1}^{n_s} \operatorname{tr}(\boldsymbol{\Sigma}_{\mathbf{c}_s})\operatorname{tr}(\boldsymbol{\Sigma}_{\mathbf{m}_s}) ,
\end{aligned}
\tag{35}
$$

$$
\operatorname{tr}(\mathbf{F}^{\mathrm{T}}\mathbf{F}\langle\mathbf{c}_s\mathbf{c}_s^{\mathrm{T}}\rangle) = \operatorname{tr}(\mathbf{F}^{\mathrm{T}}\mathbf{F}\langle\mathbf{c}_s\rangle\langle\mathbf{c}_s\rangle^{\mathrm{T}}) + \operatorname{tr}(\mathbf{F}^{\mathrm{T}}\mathbf{F}\boldsymbol{\Sigma}_{\mathbf{c}_s}) ,
\tag{36}
$$

$$
\begin{aligned}
\operatorname{tr}(\langle(\mathbf{m}_s - \underline{\mathbf{m}}_s)(\mathbf{m}_s - \underline{\mathbf{m}}_s)^{\mathrm{T}}\rangle) = \\
= \operatorname{tr}((\langle\mathbf{m}_s\rangle - \underline{\mathbf{m}}_s)(\langle\mathbf{m}_s\rangle - \underline{\mathbf{m}}_s)^{\mathrm{T}}) + \operatorname{tr}(\boldsymbol{\Sigma}_{\mathbf{m}_s}) .
\end{aligned}
\tag{37}
$$

D. Proposed algorithms

Based on the previous derivations, we propose three different algorithms. Algorithm 1, named Variational Bayesian Color Deconvolution when the ground truth color matrix is available, assumes that we have an exact knowledge of the color vector matrix $\mathbf{M}_{GT}$ and estimates, in an iterative way, the distribution of the concentrations $\mathbf{c}_s$ and the model parameters, $\hat{\beta}$ and $\hat{\boldsymbol{\alpha}}$. The proposed Variational Bayesian Blind Color Deconvolution method without prior on the color matrix, summarized in Algorithm 2, allows to obtain the estimated concentrations $\hat{\mathbf{c}}_s$ and color-vectors $\hat{\mathbf{m}}_s$ iterating on the parameters, concentration and color-vector updates until convergence, without imposing a prior distribution on the values of $\mathbf{M}$. If we include a prior distribution, we obtain Algorithm 3, Variational Bayesian Blind Color Deconvolution with prior knowledge on the color matrix. Note that this algorithm is the same as the one proposed in [24] but here it has been obtained using a framework which allows the introduction of additional information on the model parameters. Algorithms 1 and 2 are new and can be used in situations where Algorithm 3 is impractical. Finally, for all the algorithms, an RGB image of each separated stain, $\hat{\mathbf{I}}_s^{\mathrm{sep}}$, can be obtained as

$$
(\hat{\mathbf{I}}_s^{\mathrm{sep}})^{\mathrm{T}} = \exp_{10}\left(-\hat{\mathbf{m}}_s\hat{\mathbf{c}}_s^{\mathrm{T}}\right).
\tag{38}
$$

IV. MATERIALS AND METHODS

We compared the proposed approach with classical and state-of-the-art CD methods on two benchmarks: *Warwick Stain Separation Benchmark* (WSSB) in [14] and the stain separation benchmark in [9]. WSSB includes images from three datasets with different types of tissue: breast, colon and lung. The breast dataset contains three images, from different patients, from the Assessment of Mitosis Detection Algorithms (AMIDA2013) contest dataset [33]. The colon dataset contains seven images and the lung dataset has two images from different patients scanned at University Hospitals Coventry and Warwickshire [34]. From each image, two non-overlapping regions were selected. From the colon and breast images, selected regions had a size of 2000×2000 pixels at $40\times$ magnification and, from the lung images, regions had a size

---

Algorithm 1 Variational Bayesian Color Deconvolution when the ground truth color matrix is available

Require: Observed image $\mathbf{I}$, known color-vector matrix $\mathbf{M}_{GT}$.

Obtain the observed OD image, $\mathbf{Y}$, from $\mathbf{I}$ using (2), set $n = 0$, $\boldsymbol{\Sigma}_{\mathbf{c}_s}^{(0)} = \mathbf{0}$, and set $\langle\mathbf{c}_s\rangle^{(0)}$, $\forall s = 1, \ldots, n_s$, from the matrix $\mathbf{C}$ obtained as $\mathbf{C}^{\mathrm{T}} = \mathbf{M}_{GT}^{+}\mathbf{Y}^{\mathrm{T}}$, with $\mathbf{M}_{GT}^{+}$ the Moore-Penrose pseudo-inverse of $\mathbf{M}_{GT}$.

while convergence criterion is not met **do**
  1. Set $n = n + 1$.
  2. Using $\langle\mathbf{c}_s\rangle^{(n-1)}$ and $\boldsymbol{\Sigma}_{\mathbf{c}_s}^{(n-1)}$, $\forall s \in \{1, \ldots, n_s\}$, obtain the new parameter estimations $\beta^{(n)}$ and $\boldsymbol{\alpha}^{(n)}$ from (32) and (33), respectively.
  3. Using $\beta^{(n)}$ and $\alpha_s^{(n)}$ obtain the concentration updates $\boldsymbol{\Sigma}_{\mathbf{c}_s}^{(n)}$ and $\langle\mathbf{c}_s\rangle^{(n)}$ from (23), $\forall s \in \{1, \ldots, n_s\}$.
end while
Output the concentrations $\hat{\mathbf{c}}_s = \langle\mathbf{c}_s\rangle^{(n)}$, $\forall s \in \{1, \ldots, n_s\}$.

Algorithm 2 Variational Bayesian Blind Color Deconvolution without prior on the color matrix

Require: Observed image $\mathbf{I}$, initial color-vector matrix $\underline{\mathbf{M}}$.

Obtain the observed OD image, $\mathbf{Y}$, from $\mathbf{I}$ using (2), set $n = 0$, $\langle\mathbf{m}_s\rangle^{(0)} = \underline{\mathbf{m}}_s$, $\boldsymbol{\Sigma}_{\mathbf{m}_s}^{(0)} = \mathbf{0}$, $\boldsymbol{\Sigma}_{\mathbf{c}_s}^{(0)} = \mathbf{0}$, $\langle\mathbf{c}_s\rangle^{(0)}$, $\forall s = 1, \ldots, n_s$, from the matrix $\mathbf{C}$ obtained as $\mathbf{C}^{\mathrm{T}} = \underline{\mathbf{M}}^{+}\mathbf{Y}^{\mathrm{T}}$, with $\underline{\mathbf{M}}^{+}$ the Moore-Penrose pseudo-inverse of $\underline{\mathbf{M}}$.

while convergence criterion is not met **do**
  1. Set $n = n + 1$.
  2. Using $\langle\mathbf{m}_s\rangle^{(n-1)}$, $\boldsymbol{\Sigma}_{\mathbf{m}_s}^{(n-1)}$, $\langle\mathbf{c}_s\rangle^{(n-1)}$ and $\boldsymbol{\Sigma}_{\mathbf{c}_s}^{(n-1)}$, $\forall s \in \{1, \ldots, n_s\}$, obtain the new parameter estimations $\beta^{(n)}$ and $\boldsymbol{\alpha}^{(n)}$ from (32) and (33), respectively.
  3. Using $\beta^{(n)}$, $\alpha_s^{(n)}$, $\langle\mathbf{m}_s\rangle^{(n-1)}$ and $\boldsymbol{\Sigma}_{\mathbf{m}_s}^{(n-1)}$ obtain the concentration updates $\boldsymbol{\Sigma}_{\mathbf{c}_s}^{(n)}$ and $\langle\mathbf{c}_s\rangle^{(n)}$ from (23), $\forall s \in \{1, \ldots, n_s\}$.
  4. Using $\beta^{(n)}$, $\langle\mathbf{c}_s\rangle^{(n)}$ and $\boldsymbol{\Sigma}_{\mathbf{c}_s}^{(n)}$ obtain the color-vector update $\boldsymbol{\Sigma}_{\mathbf{m}_s}^{(n)}$ and $\langle\mathbf{m}_s\rangle^{(n)}$ from (29), $\forall s \in \{1, \ldots, n_s\}$.
end while
Output the color-vector $\hat{\mathbf{m}}_s = \langle\mathbf{m}_s\rangle^{(n)}$ and the concentrations $\hat{\mathbf{c}}_s = \langle\mathbf{c}_s\rangle^{(n)}$, $\forall s \in \{1, \ldots, n_s\}$.

---

of 500×500 pixels at $20\times$ magnification. This makes a total of 24 samples all stained with H&E. An H&E stained image in the lung dataset is shown in Fig. 1(a). In [14], the reference ground truth stain color-vector matrices, $\mathbf{M}_{GT}$, were obtained as follows: for each image, a set of pixels for H and for E were manually selected based on biological structure rather than stain color, that is, pixels belonging to nuclei were selected as reference for H stain and cytoplasm pixels as reference for E stain. For each image and stain, the median in OD space of the selected pixels was taken as the ground truth color vector. Given those color-vector matrices, ground truth concentrations were derived in [14] as $\mathbf{C}_{GT}^{\mathrm{T}} = \mathbf{M}_{GT}^{+}\mathbf{Y}^{\mathrm{T}}$. From those concentrations, the corresponding ground truth RGB stain separated images were obtained by applying (38). Figs. 1(b) and 1(c) show, respectively, the ground truth RGB separated H-only and E-only images for the observed H&E image in Fig. 1(a).
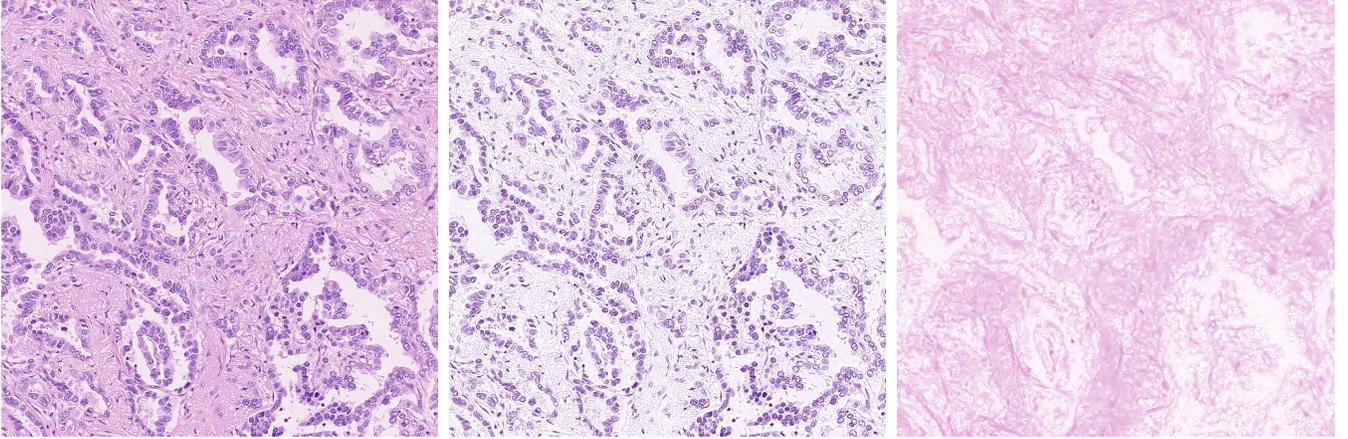
a) H&E image   b) Ground truth separated H-only image c) Ground truth separated E-only image

Fig. 1. Lung observed H&E image from the WSSB dataset in [14] and its separated ground truth H-only and E-only images.

Algorithm 3 Variational Bayesian Blind Color Deconvolution with prior knowledge on the color matrix

---

Require: Observed image $\mathbf{I}$, reference (prior) color-vector matrix $\underline{\mathbf{M}}$.

Obtain the observed OD image, $\mathbf{Y}$, from $\mathbf{I}$ using (2) and set $\langle \mathbf{m}_s \rangle^{(0)} = \underline{\mathbf{m}_s}$, $\boldsymbol{\Sigma}_{\mathbf{m}_s}^{(0)} = \mathbf{0}$, $\boldsymbol{\Sigma}_{\mathbf{c}_s}^{(0)} = \mathbf{0}$, $\langle \mathbf{c}_s \rangle^{(0)}$, $\forall s = 1, \ldots, n_s$, from the matrix $\mathbf{C}$ obtained as $\mathbf{C}^{\mathrm{T}} = \underline{\mathbf{M}}^{+} \mathbf{Y}^{\mathrm{T}}$, with $\underline{\mathbf{M}}^{+}$ the Moore-Penrose pseudo-inverse of $\underline{\mathbf{M}}$, and $n = 0$.

while convergence criterion is not met **do**

    1. Set $n = n + 1$.

    2. Using $\langle \mathbf{m}_s \rangle^{(n-1)}$, $\boldsymbol{\Sigma}_{\mathbf{m}_s}^{(n-1)}$, $\langle \mathbf{c}_s \rangle^{(n-1)}$ and $\boldsymbol{\Sigma}_{\mathbf{c}_s}^{(n-1)}$, $\forall s \in \{1, \ldots, n_s\}$, obtain the new parameter estimations $\beta^{(n)}$, $\boldsymbol{\alpha}^{(n)}$ and $\boldsymbol{\gamma}^{(n)}$ from (32), (33) and (34), respectively.

    3. Using $\beta^{(n)}$, $\alpha_s^{(n)}$, $\langle \mathbf{m}_s \rangle^{(n-1)}$ and $\boldsymbol{\Sigma}_{\mathbf{m}_s}^{(n-1)}$ obtain the concentration updates $\boldsymbol{\Sigma}_{\mathbf{c}_s}^{(n)}$ and $\langle \mathbf{c}_s \rangle^{(n)}$ from (23), $\forall s \in \{1, \ldots, n_s\}$.

    4. Using $\beta^{(n)}$, $\gamma_s^{(n)}$, $\langle \mathbf{c}_s \rangle^{(n)}$ and $\boldsymbol{\Sigma}_{\mathbf{c}_s}^{(n)}$ obtain the color-vector update $\boldsymbol{\Sigma}_{\mathbf{m}_s}^{(n)}$ and $\langle \mathbf{m}_s \rangle^{(n)}$ from (29), $\forall s \in \{1, \ldots, n_s\}$.

end while

Output the color-vector $\hat{\mathbf{m}}_s = \langle \mathbf{m}_s \rangle^{(n)}$ and the concentrations $\hat{\mathbf{c}}_s = \langle \mathbf{c}_s \rangle^{(n)}$, $\forall s \in \{1, \ldots, n_s\}$.

The benchmark dataset in [9] is formed by three H&E stained images of size 1024×1280 and their corresponding H-only and E-only images are used as ground truth images for testing color deconvolution procedures. Each image in the dataset was obtained by first eosin staining the tissue, imaging, destaining, staining again, now with hematoxylin, imaging, staining with eosin too and imaging. An example of H&E stained image in the dataset is shown in Fig. 3(a) and its corresponding E-only and H-only images are shown on the left and right hand sides of Fig. 3(b), respectively. The staining-destaining process of the slides of this dataset caused slight tissue motions and deformations. These deformations were partially corrected in [9] by geometrically registering the H-only and E-only images to their corresponding H&E image.

The proposed algorithms were run, for all benchmark datasets, until the stopping criterion $\| \langle \mathbf{c}_s \rangle^{(n)} - \langle \mathbf{c}_s \rangle^{(n-1)} \|^2 / \| \langle \mathbf{c}_s \rangle^{(n)} \|^2 < 10^{-5}$ for both stains, that is, $s = 1, 2$, was met. Since the images in the WSSB dataset in [14] come from different tissues and have different characteristics, we fixed the reference color-vector matrix $\underline{\mathbf{M}}$ by selecting, for each tissue type: breast, colon, and lung, a single pixel containing mainly hematoxylin and another pixel containing mainly eosin.

We have compared the proposed methods against the non-blind color deconvolution method in [4], the classical blind method in [5] and the recent methods in [9], [11] and [14]. For all the competing algorithms, parameters were selected following the recommendations on the original paper or the reference software freely available.

For the two considered benchmark datasets, WSSB [14] and the one in [9], *Peak Signal to Noise Ratio* (PSNR) and *Structural Similarity* (SSIM) [35] between the reconstructed H- and E-images and their corresponding ground truth images are provided. Images, for visual comparison, have also been included. For the WSSB dataset, where the ground-truth color-vectors are available the *Euclidean Distances* (EDs) between the ground truth color-vectors and the color-vectors obtained using the different methods have been computed.

V. RESULTS

First, we show the proposed and competing methods performance on the WSSB dataset in [14]. Table I shows the numerical results of applying the proposed Alg. 2, that is, not including a prior on the color-vectors, to this dataset. Results show high PSNR values with a mean value of 28.63dB for the H-only image and 26.44dB for the E-only image. SSIM figures-of-merit are also remarkably high with all the values above 0.9 and mean values of almost 0.95 for the hematoxylin and more than 0.91 for the eosin. These figures are higher than all the obtained by the competing methods. When prior information on the color-vectors is included, that is, when Alg. 3 is used, better numerical results are obtained for all the

TABLE I
PSNR AND SSIM FOR THE DIFFERENT METHODS AND STAIN IMAGES OF THE WSSB DATASET [14].

Image	Stain	Method in [4]		Method in [5]		Method in [9]		Method in [11]		Method in [14]		Alg. 2		Alg. 3		Alg. 1	
		PSNR	SSIM	PSNR	SSIM	PSNR	SSIM	PSNR	SSIM	PSNR	SSIM	PSNR	SSIM	PSNR	SSIM	PSNR	SSIM
Colon	H	22.27	0.8141	23.91	0.8095	24.72	0.9100	25.83	0.8851	21.11	0.7241	28.32	0.9516	**28.57**	**0.9542**	34.55	0.9782
	E	20.70	0.7456	21.55	0.6365	21.87	0.7905	26.29	0.8904	21.94	0.8540	26.50	0.9020	**27.58**	**0.9139**	33.89	0.9518
Breast	H	15.27	0.6215	26.24	0.9552	23.89	0.8748	25.46	0.9239	24.60	0.8068	27.22	0.9359	**28.81**	**0.9528**	33.46	0.9758
	E	17.66	0.7644	23.62	0.9336	19.81	0.8663	27.68	0.9550	25.92	0.9380	25.31	0.9339	**26.60**	**0.9464**	33.05	0.9778
Lung	H	22.47	0.7987	19.52	0.7389	26.88	0.9318	25.87	0.8912	20.62	0.5551	30.36	0.9596	**32.91**	**0.9763**	37.12	0.9857
	E	22.05	0.7734	18.09	0.5088	24.15	0.8539	25.53	0.8195	23.95	0.8939	27.52	0.9110	**30.77**	**0.9306**	35.57	0.9634
Mean	H	20.00	0.7448	23.22	0.8345	25.16	0.9022	25.72	0.9100	22.11	0.6953	28.63	0.9490	**30.10**	**0.9611**	35.05	0.9799
	E	20.14	0.7611	21.08	0.6930	21.94	0.8369	26.50	0.8883	23.94	0.8953	26.44	0.9156	**28.32**	**0.9303**	34.17	0.9643

TABLE II
EUCLIDEAN DISTANCE BETWEEN WSSB GROUND TRUTH COLOR-VECTORS [14] AND ESTIMATED ONES.

Image	Stain	Method in [4]	Method in [5]	Method in [9]	Method in [11]	Method in [14]	Alg. 2	Alg. 3
Colon	H	0.8131	0.0765	0.1216	**0.0329**	0.2361	0.0504	0.0564
	E	0.5883	0.2010	0.2333	**0.0689**	0.1997	0.1401	0.1012
Breast	H	0.7421	0.1213	0.1531	**0.0378**	0.1015	0.0948	0.0660
	E	0.8090	0.0672	0.1291	**0.0496**	0.1748	0.0721	0.0683
Lung	H	0.7861	0.1862	0.0834	0.0654	0.2116	0.1012	**0.0415**
	E	0.6116	0.3089	0.2697	0.1312	0.0944	0.0791	**0.0374**
Mean	H	0.7804	0.1280	0.1194	**0.0454**	0.1831	0.0821	0.0546
	E	0.6696	0.1924	0.2107	0.0832	0.1563	0.0971	**0.0689**

images. A mean increment of almost 2dB in PSNR and almost 0.15 in SSIM are obtained for the whole dataset. We note that all the compared blind color deconvolution methods produce better numerical results than those of the non-blind method in [4], being specially relevant the ones obtained by the method in [11], although they are still far from those produced by the proposed methods. Note also that the methods in [11] and in [14] tend to better estimate the eosin image while the proposed methods and the other methods usually get better results for the hematoxylin stain. We want to note here that the method in [14] usually tends to confuse hematoxylin with background and we had to manually check which image corresponded to each stain. Without this manual correction, the mean PSNR and SSIM figures-of-merit for the H-only image were only 16.85dB and 0.5827. Table I also shows the results of applying the proposed non-blind Alg. 1 with the ground truth vectors, $\mathbf{M}_{GT}$, obtained in [14] for this dataset. The results, that show the highest values both for PSNR and SSIM, provide an upper bound for those measures. Note that the obtained values are much higher than those obtained by all the other methods meaning that there are still room for improvement both in PSNR and, to a less extent, in SSIM.

Table II shows the ED between the ground truth color-vectors, $\mathbf{M}_{GT}$, and those obtained by the different methods. Alg. 1 is not included in Table II because in this algorithm $\mathbf{M}_{GT}$ has been directly used. The largest ED values in Table II correspond to [4] which uses always the same color-vector matrices (for all the slides), followed by the methods in [14], [9] and [5]. The method in [11] obtains the smallest distances to the ground truth in almost all cases, except for lung slides and the mean value for eosin color-vectors. In these cases the proposed Alg. 3 outperforms the method in [11] and in the rest of the cases obtains ED values very close to those of [11]. The proposed algorithms obtain better results than the other methods, except the method in [11], and the method in [5] for

the eosin color-vector of breast slides. Algorithm 2 produces slightly worse results than Alg. 3 for this dataset, but they are much better than the ones of the competing methods. Note that both Alg. 2 and Alg. 3, and the method in [11] also showed better results than the rest of methods in terms of PSNR and SSIM (see Table I). As it was expected, a good estimation of the color-vector matrix improves stain separation results.

Visually, the proposed methods produce images that are much closer to the ground truth images (see Fig. 2) than those of the competitors. The proposed non-blind Alg. 1 with the ground truth vectors produces images almost indistinguishable from the ground truth ones. The proposed Alg. 3 produces images very close to the ground truth, both for the H and E separations while the proposed Alg. 2 produces slightly not so accurate colors. From the depicted images it is clear that the classical method in [5] produced the worst separation, including almost all the structures into the H-only image. The non-blind method in [4], Fig. 2b, produces better results although colors are not close to the ground truth ones. The method in [14] confuses hematoxylin with background. We manually corrected this to show the images in Fig. 2f. Although nuclei are clearly differentiated in the H-only image, part of the smaller structures are missing and the eosin color are more saturated than those of the ground truth image. The method in [9] and the method in [11] produce good differentiated nuclei, and a good approximation for the eosin channel, see in particular the method in [11]. However, they are all outperformed by the proposed methods.

We have also tested the proposed approaches and the other methods on the stain separation benchmark in [9]. Figure 3a shows the first image in the dataset. The ground truth separation for this image is shown in Figure 3b. The E-only image is shown on the left-hand side of the image while the H-only image is depicted on the right-hand side. Note that the position of the tissue is not exactly the same

for both stains (left and right images do not exactly match) and that there are differences with the observed image. For instance, the structure at the bottom center of the image is folded in the observed image. Those differences are due to the process to obtain the observed and ground truth images previously described. Geometrically registering the images partially solved these problems [9]. Figures 3c-i show the separations with the proposed and competing methods. From the images, it is clear that the method in [9] and the proposed algorithms produce results closer to the ground truth than the methods in [4], [5], [11] and [14]. The proposed methods and the method in [9], extract nuclei and other structures present in both stains but ours seem closer to the ground truth. Note, for instance, that the long structure in the center of the image (corresponding to bone tissue [9]) is not clearly shown in the hematoxylin estimations in Figs. 3c, 3d, 3f and 3g. All eosin estimations have a higher contrast than the ground truth although estimations obtained by the proposed methods and the method in [9] are more similar to the ground truth. The eosin estimation by the method in [9] seems to be slightly less contrasted than the one by the proposed algorithms. In this case, the eosin estimation obtained by the proposed Alg. 3 seems not so close to the ground truth as the one obtained by Alg. 2. However, the hematoxylin estimation obtained by the proposed Alg. 3 seems slightly closer to the ground truth image than the obtained by Alg. 2. Note that we have not run Alg 1 since we do not know the ground truth color vectors for this dataset.

Numerical results, using PSNR and SSIM measures, for the proposed and competing methods are presented in Table III. The figures-of-merit confirm the visual inspection results. The proposed methods perform better than the competitors, except for the case of the eosin stain for the algorithm in [9]. This was expected since this algorithm selectively modifies the initially obtained values for the stain separations to better accommodate ground truth. More precisely, in [9] the eosin separation is corrected in contrast by adding a small part of the hematoxylin stain, and the hematoxylin stain is then computed again by taking into account interaction between the stains in those places where the contrast of the eosin coefficients has been adjusted. Note that, in spite of these adjustments, the proposed methods consistently provide better PSNR results for the hematoxylin stain than the method in [9]. Notice that all the PSNR and, especially, the SSIM values in Table III are quite low. This is due to the staining-destaining process that makes the tissue to move and deform. Although, for all the experiments, we used the registered images from [9] as ground truth, there still are some misalignments between ground truth and estimations that deteriorate the figures-of-merit.

In this database, the proposed Alg. 2 took 8s on a i7-8550U @ 1.80GHz laptop with 16 GB RAM and the proposed Alg. 3 took only 5s. Obviously, including prior information on the color-vectors makes the algorithm to converge faster, with a very low increase of the computational burden. In comparison, the recent methods in [9], [11] and [14] needed around 1s, 25s and 5s, respectively. The classical method in [5], as well as the non-blind color deconvolution method in [4] are much faster, needing less than 1s per image. We note

that the proposed method not only estimates the color-vectors and stain separations but all the model parameters while the rest of the methods need to manually tune them.

VI. CONCLUSIONS

A novel variational Bayesian blind color deconvolution framework for histological images has been developed. Three algorithms have been proposed depending on the information we have on the color-vectors. All of them estimate the color-vector matrix (for the first algorithm it is provided by the user), the concentration of the stains and all the model parameters. They take into account the spatial relations between pixels as well as, in the case of Alg. 3, the similarity to a reference color-vector matrix. Comparison with classical and recent methods demonstrated that our approach produces better results than the competitors, except for the PSNR of the eosin stain by the algorithm in [9] in their dataset and the algorithm in [11] for the ED to the ground truth color-vectors, as already mentioned. Computing time is also competitive, specially taking into account that the proposed method automatically estimate all the model parameters.

REFERENCES

[1] A. Rabinovich, S. Agarwal, C. Laris, J. H. Price, and S. J. Belongie, "Unsupervised color decomposition of histologically stained tissue samples," in *Advances in neural information processing systems*, 2004, pp. 667–674.

[2] C. R. Taylor and R. M. Levenson, "Quantification of immunohistochemistry—issues concerning methods, utility and semiquantitative assessment II," *Histopathology*, vol. 49, no. 4, pp. 411–424, 2006.

[3] S. Roy, A. kumar Jain, S. Lal, and J. Kini, "A study about color normalization methods for histopathology images," *Micron*, vol. 114, pp. 42–61, Nov. 2018.

[4] A. C. Ruifrok and D. A. Johnston, "Quantification of histochemical staining by color deconvolution," *Analytical and quantitative cytology and histology*, vol. 23, no. 4, pp. 291–299, 2001.

[5] M. Macenko, M. Niethammer, J. S. Marron, D. Borland, J. T. Woosley, X. Guan, C. Schmitt, and N. E. Thomas, "A method for normalizing histology slides for quantitative analysis," in *2009 IEEE International Symposium on Biomedical Imaging: From Nano to Macro*, 2009, pp. 1107–1110.

[6] M. Gavrilovic, J. C. Azar, J. Lindblad, C. Wählby, E. Bengtsson, C. Busch, and I. B. Carlbom, "Blind Color Decomposition of Histological Images," *IEEE Transactions on Medical Imaging*, vol. 32, no. 6, pp. 983–994, Jun. 2013.

[7] A. M. Khan, N. Rajpoot, D. Treanor, and D. Magee, "A Nonlinear Mapping Approach to Stain Normalization in Digital Histopathology Images Using Image-Specific Color Deconvolution," *IEEE Transactions on Biomedical Engineering*, vol. 61, no. 6, pp. 1729–1738, 2014.

[8] B. E. Bejnordi, G. Litjens, N. Timofeeva, I. Otte-Höller, A. Homeyer, N. Karssemeijer, and J. A. v. d. Laak, "Stain Specific Standardization of Whole-Slide Histopathological Images," *IEEE Transactions on Medical Imaging*, vol. 35, no. 2, pp. 404–415, Feb. 2016.

[9] M. T. McCann, J. Majumdar, C. Peng, C. A. Castro, and J. Kovačević, "Algorithm and benchmark dataset for stain separation in histology images," in *IEEE International Conference on Image Processing (ICIP)*, 2014, pp. 3953–3957.

[10] J. Xu, L. Xiang, G. Wang, S. Ganesan, M. Feldman, N. N. C. Shih, H. Gilmore, and A. Madabhushi, "Sparse Non-negative Matrix Factorization (SNMF) based color unmixing for breast histopathological image analysis," *Computerized Medical Imaging and Graphics*, vol. 46, pp. 20–29, Dec. 2015.

[11] A. Vahadane, T. Peng, A. Sethi, S. Albarqouni, L. Wang, M. Baust, K. Steiger, A. M. Schlitter, I. Esposito, and N. Navab, "Structure-preserving color normalization and sparse stain separation for histological images," *IEEE Transactions on Medical Imaging*, vol. 35, no. 8, pp. 1962–1971, Aug. 2016.

TABLE III
PSNR AND SSIM FOR THE DIFFERENT METHODS AND IMAGES OF THE DATASET IN [9].

Image	Stain	Method in [4]		Method in [5]		Method in [9]		Method in [11]		Method in [14]		Alg. 2		Alg. 3	
		PSNR	SSIM	PSNR	SSIM	PSNR	SSIM	PSNR	SSIM	PSNR	SSIM	PSNR	SSIM	PSNR	SSIM
HE1	H	17.07	0.4275	17.35	0.4304	18.20	0.4614	16.56	0.3745	16.49	0.3964	18.34	0.4710	**18.38**	**0.4769**
	E	18.44	0.6675	18.70	0.6816	**20.04**	**0.6964**	18.17	0.6248	17.97	0.5506	19.40	0.6927	19.23	0.6760
HE2	H	16.21	0.4200	16.75	0.4578	17.52	0.4662	16.16	0.3945	15.87	0.3979	17.64	0.4564	**17.70**	**0.4881**
	E	17.15	0.6592	17.54	0.6850	**19.37**	**0.7008**	17.08	0.6593	16.92	0.4843	18.20	0.6950	18.01	0.6738
HE3	H	16.89	0.4660	17.33	0.4724	18.54	0.5241	16.53	0.4106	16.55	0.4580	**18.63**	**0.5285**	18.61	0.5234
	E	17.79	0.6905	18.12	0.7247	**20.29**	0.7158	17.57	0.6732	16.91	0.6652	19.01	**0.7301**	18.94	0.7179
Mean	H	16.72	0.4379	17.14	0.4535	18.09	0.4839	16.42	0.3932	16.30	0.4174	18.20	0.4853	**18.23**	**0.4961**
	E	17.79	0.6724	18.12	0.6971	**19.90**	0.7043	17.61	0.6525	17.27	0.5667	18.87	**0.7059**	18.73	0.6892

[12] D. Carey, V. N. Wijayathunga, A. J. Bulpitt, and D. Treanor, "A novel approach for the colour deconvolution of multiple histological stains," in *Proceedings of the 19th Conference of Medical Image Understanding and Analysis*, 2015, Proceedings Paper, pp. 156–162.

[13] N. Alsubaie, S. E. A. Raza, and N. Rajpoot, "Stain deconvolution of histology images via independent component analysis in the wavelet domain," in *2016 IEEE 13th International Symposium on Biomedical Imaging (ISBI)*, 2016, pp. 803–806.

[14] N. Alsubaie, N. Trahearn, S. E. A. Raza, D. Snead, and N. M. Rajpoot, "Stain deconvolution using statistical analysis of multi-resolution stain colour representation," *PLOS ONE*, vol. 12, no. 1, p. e0169875, Jan. 2017.

[15] N. Trahearn, D. Snead, I. Cree, and N. Rajpoot, "Multi-class stain separation using independent component analysis," in *Medical Imaging 2015: Digital Pathology*, 2015, p. 94200J.

[16] L. Astola, "Stain separation in digital bright field histopathology," in *2016 Sixth International Conference on Image Processing Theory, Tools and Applications (IPTA)*, 2016, pp. 1–6.

[17] Y. Zheng, Z. Jiang, H. Zhang, F. Xie, J. Shi, and C. Xue, "Adaptive color deconvolution for histological WSI normalization," *Computer Methods and Programs in Biomedicine*, vol. 170, pp. 107–120, Mar. 2019.

[18] R. Duggal, A. Gupta, R. Gupta, and P. Mallick, "SD-layer: stain deconvolutional layer for CNNs in medical microscopic imaging," in *International Conference on Medical Image Computing and Computer-Assisted Intervention*. Springer, 2017, pp. 435–443.

[19] A. Lahiani, J. Gildenblat, I. Klaman, N. Navab, and E. Klaiman, "Generalising multistain immunohistochemistry tissue segmentation using end-to-end colour deconvolution deep neural networks," *IET Image Processing*, vol. 13, no. 7, pp. 1066–1073, Feb. 2019.

[20] A. Janowczyk, A. Basavanhally, and A. Madabhushi, "Stain normalization using sparse autoencoders (StaNoSA): Application to digital pathology," *Computerized Medical Imaging and Graphics*, vol. 57, pp. 50–61, 2017.

[21] F. G. Zanjani, S. Zinger, B. E. Bejnordi, J. A. W. M. v. d. Laak, and P. H. N. d. With, "Stain normalization of histopathology images using generative adversarial networks," in *2018 IEEE 15th International Symposium on Biomedical Imaging (ISBI 2018)*, Apr. 2018, pp. 573–577.

[22] M. T. Shaban, C. Baur, N. Navab, and S. Albarqouni, "StainGAN: Stain style transfer for digital histological images," in *2019 IEEE 16th International Symposium on Biomedical Imaging (ISBI 2019)*, Apr. 2019, pp. 953–956.

[23] N. Hidalgo-Gavira, J. Mateos, M. Vega, R. Molina, and A. Katsaggelos, "Fully automated blind color deconvolution of histopathological images," in *21st International Conference on Medical Image Computing and Computer Assisted (MICCAI 2018)*, Sep. 2018, pp. 183–191.

[24] ——, "Blind color deconvolution of histopathological images using a variational Bayesian approach," in *IEEE International Conference on Image Processing (ICIP 2018)*, Oct. 2018, pp. 983–987.

[25] Z. Chen, S. D. Babacan, R. Molina, and A. K. Katsaggelos, "Variational Bayesian methods for multimedia problems," *IEEE Transaction on Multimedia*, vol. 16, no. 4, pp. 1000–1017, 2014.

[26] M. Beal, "Variational algorithms for approximate Bayesian inference," Ph.D. dissertation, The Gatsby Computational Neuroscience Unit, University College London, 2003.

[27] M. Luessi, S. Babacan, R. Molina, J. Booth, and A. Katsaggelos, "Bayesian symmetrical EEG/fMRI fusion with spatially adaptive priors." *NeuroImage,*, vol. 55, no. 1, pp. 113–132, 2011.

[28] ——, "Variational Bayesian causal connectivity analysis for fMRI," *Frontiers in Neuroinformatics*, vol. 8, no. 45, 2014.

[29] R. Molina and B. Ripley, "Using spatial models as priors in astronomical image analysis," *Journal of Applied Statistics*, vol. 16, pp. 193–206, 1989.

[30] A. Katsaggelos, R. Molina, and J. Mateos, *Super resolution of images and video*, ser. Synthesis Lectures on Image, Video, and Multimedia Processing. Morgan & Claypool, 2007.

[31] P. Ruiz, X. Zhou, J. Mateos, R. Molina, and A. Katsaggelos, "Variational Bayesian blind image deconvolution: A review," *Digital Signal Processing*, vol. 47, pp. 116–127, December 2015.

[32] C. Bishop, *Pattern Recognition and Machine Learning*. Springer, 2006, pp. 454–455.

[33] M. Veta, P. J. van Diest, S. M. Willems, H. Wang, A. Madabhushi, A. Cruz-Roa, F. Gonzalez, A. B. Larsen, J. S. Vestergaard, A. B. Dahl, D. C. Cireşan, J. Schmidhuber, A. Giusti, L. M. Gambardella, F. B. Tek, T. Walter, C.-W. Wang, S. Kondo, B. J. Matuszewski, F. Precioso, V. Snell, J. Kittler, T. E. de Campos, A. M. Khan, N. M. Rajpoot, E. Arkoumani, M. M. Lacle, M. A. Viergever, and J. P. Pluim, "Assessment of algorithms for mitosis detection in breast cancer histopathology images," *Medical image analysis*, vol. 20, no. 1, pp. 237–248, 2015.

[34] K. Sirinukunwattana, S. E. A. Raza, Y.-W. Tsang, D. Snead, I. Cree, and N. Rajpoot, "A spatially constrained deep learning framework for detection of epithelial tumor nuclei in cancer histology images," in *International Workshop on Patch-based Techniques in Medical Imaging*. Springer, 2015, pp. 154–162.

[35] Z. Wang, A. C. Bovik, H. R. Sheikh, and E. P. Simoncelli, "Image quality assessment: from error visibility to structural similarity," *IEEE Transactions on Image Processing*, vol. 13, no. 4, pp. 600–612, April 2004.
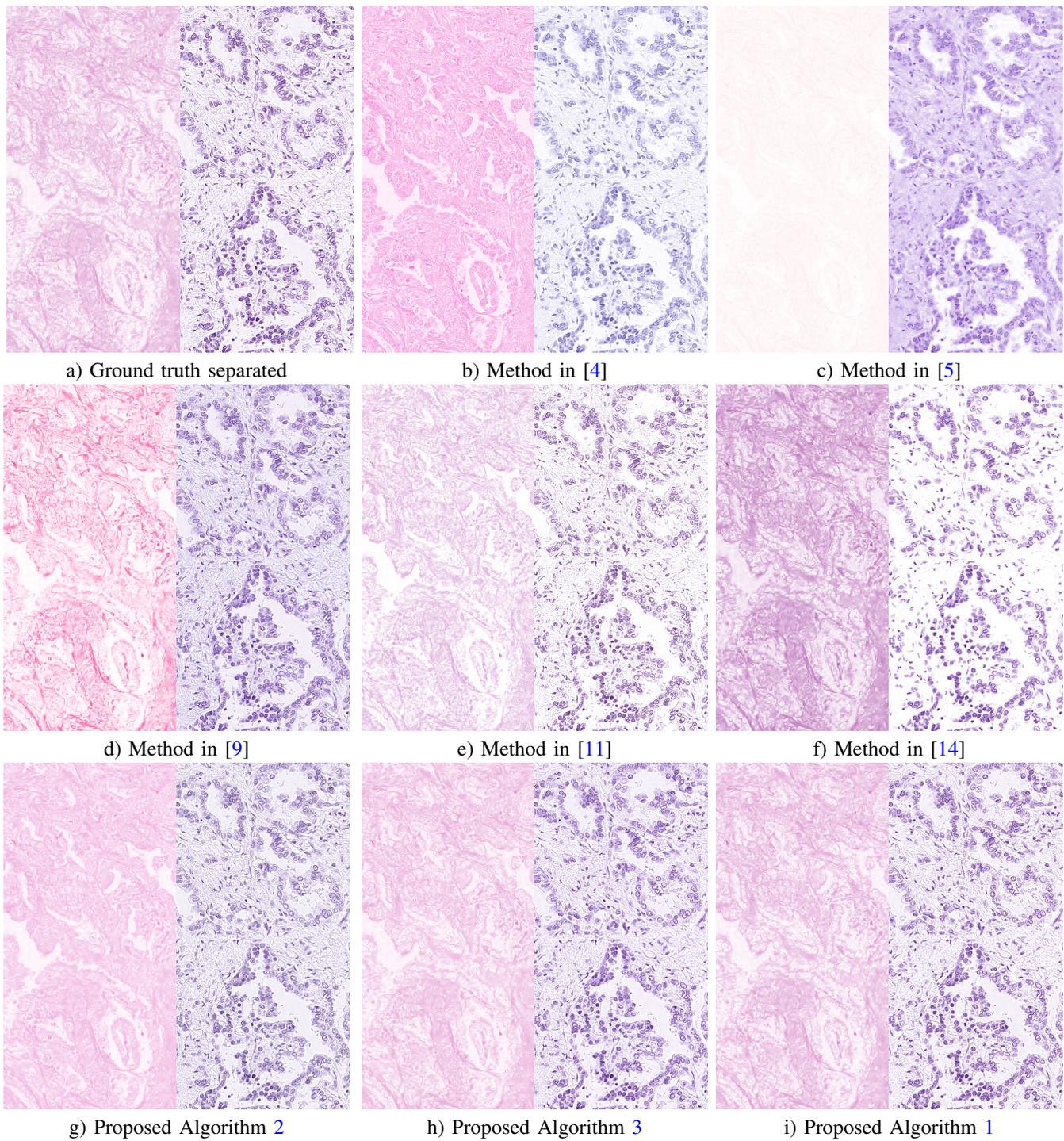
Fig. 2. Ground truth image and results by the competing and proposed methods on the lung image in Figure 1a. Recovered eosin and hematoxylin images are presented on the left and right hand sides of each image, respectively.

a) H&E image

b) E (left) and H (right) Ground truth

c) Method in [4]

d) Method in [5]

e) Method in [9]

f) Method in [11]

g) Method in [14]

h) Proposed Algorithm 2

i) Proposed Algorithm 3
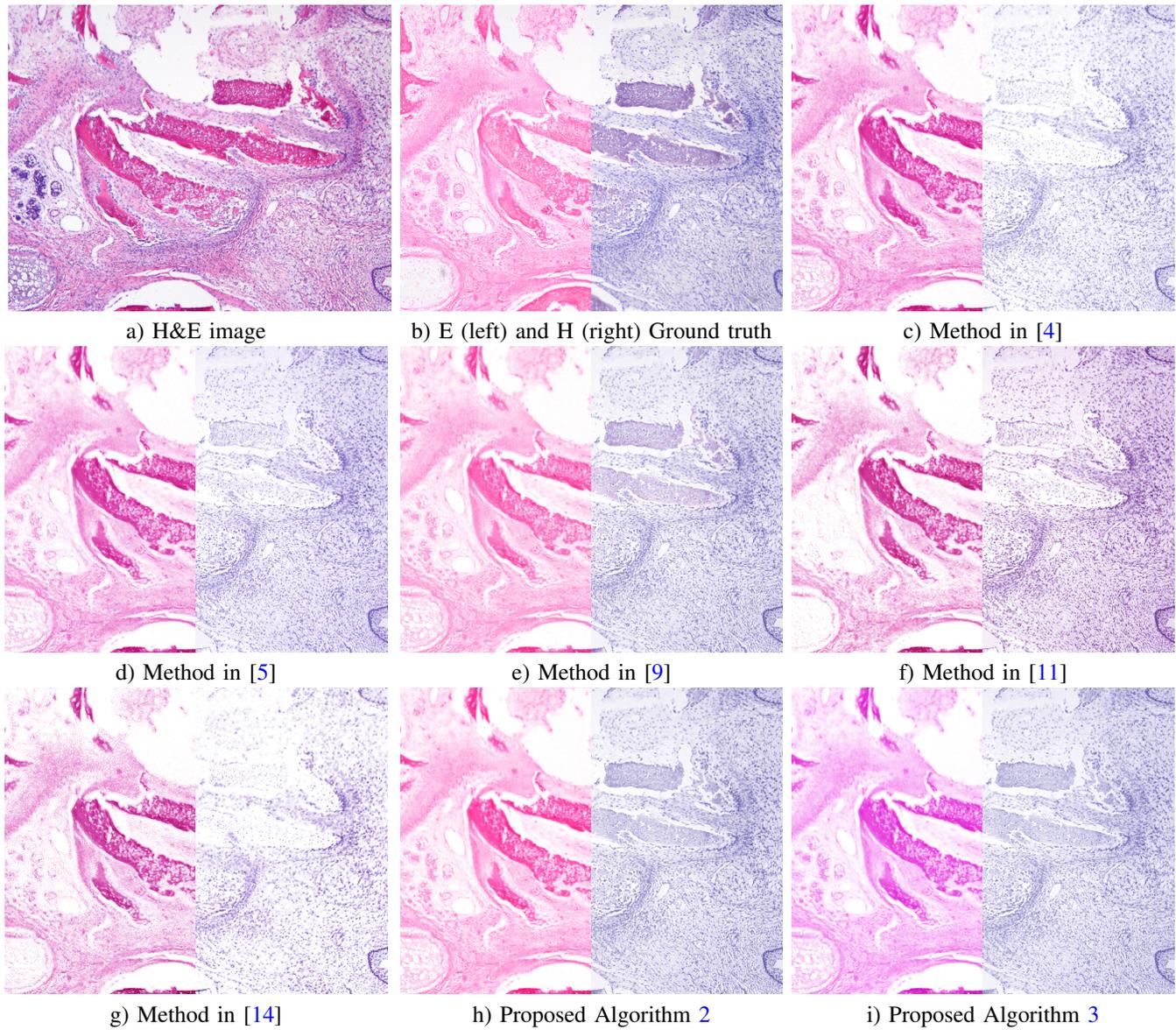
Fig. 3. Observed image 1 of the dataset in [9], ground truth separations and results obtained by competitors and the proposed methods. Recovered eosin and hematoxylin images are presented on the left and right hand sides of each image, respectively.